

Research Article

Vehicular Channel in Urban Environments at 23 GHz for Flexible Access Common Spectrum Application

Longhe Wang ^{1,2}, Bo Ai ^{1,2}, Jingya Yang ^{1,2}, Hao Qiu,^{1,2} Wanqiao Wang ^{1,2},
and Ke Guan ^{1,2}

¹State Key Laboratory of Rail Traffic Control and Safety, Beijing Jiaotong University, Beijing 100044, China

²Beijing Engineering Research Center of High-Speed Railway Broadband Mobile Communications, Beijing 100044, China

Correspondence should be addressed to Bo Ai; boai@bjtu.edu.cn

Received 3 May 2019; Accepted 30 July 2019; Published 12 September 2019

Guest Editor: Marko Sonkki

Copyright © 2019 Longhe Wang et al. This is an open access article distributed under the Creative Commons Attribution License, which permits unrestricted use, distribution, and reproduction in any medium, provided the original work is properly cited.

With the development of the vehicular network, new radio technologies have been in the spotlight for maximizing the utilization of the limited radio spectrum resource while accommodating the increasing amount of services and applications in the wireless mobile networks. New spectrum policies based on dynamic spectrum access technology such as flexible access common spectrum (FACS) have been adopted by the Korea Communications Commission (KCC). 23 GHz bands have been allocated to FACS bands by the KCC, which is expected extensively for vehicular communications. The comprehensive knowledge on the radio channel is essential to effectively support the design, simulation, and development of such radio technologies. In this paper, the characteristics of 23 GHz vehicle-to-infrastructure (V2I) channels are simulated and extracted for the urban environment in Seoul. The path loss, shadow factor, Ricean K -factor, root-mean-square (RMS) delay spread, and angular spreads are characterized from the calibrated ray-tracing simulation results, and it can help researchers have a better understanding of the propagation channel for designing vehicular radio technologies and a communication system in a similar environment.

1. Introduction

Recently, flexible access common spectrum (FACS) has been considered to have an important role in accommodating the fast-growing spectrum demands in vehicular communications, which will ramp up the development of mobile and wireless vehicular communication technologies to advance safety and convenience on the roads [1, 2]. Among them, vehicle-to-infrastructure (V2I) robust connectivity is the key enabler for enhancing traffic safety, reliability, and efficiency [3, 4]. The channel characteristic is a critical role in the design and performance evaluation of V2I connectivity networks. For example, the realistic large-scale fading channel parameters are indispensable for efficient network deployment and optimization; the fidelity small-scale fading channel parameters are crucial in physical layer design, such as optimal modulation, coding, diversity, and protocol scheme development [5].

Most of the previous works on vehicular propagation channels are focused on the 5 GHz band, e.g., [6–16], which use the lower frequency band to increase the V2I and vehicle-to-vehicle (V2V) link ranges. In [6], based on the narrowband channel measurement at 5.2 GHz, the propagation loss (PL) parameters of the vehicular channel are studied under a highway and under urban, suburban, and village environments. In [7], a large number of vehicular narrowband channel measurements are carried out at 5.9 GHz. A dual-slope PL model is proposed for the suburban environment. Meanwhile, it is found that, in such an environment, the small-scale fading of the channel obeys the Nakagami distribution, and the effect of speed and relative distance of the transmitting and receiving vehicles on the Doppler spectrum and quasistationary time is discussed. Based on the wideband multi-input multioutput (MIMO) channel measurement at the 5.3 GHz band, the authors in [8, 9] discuss the nonstationary delay spread (DS) and small-

scale fading characteristics (following Ricean distribution) in vehicular channels. In [10], under a highway environment, the PL, delay distribution, and Doppler characteristics of the V2I channel are studied according to the MIMO channel measurement. Similarly, the dispersion of multipath components (MPCs) in delay and Doppler domains is analyzed for V2I channels under urban and rural environments, and the geometry of scatterers is also being constructed to illustrate the MPC distribution [11, 12]. Moreover, in [13], the authors present a three-dimensional (3D) distribution estimation of MPCs and discuss the power ratio of different propagation mechanisms associated with the actual propagation environment. The work in [14–16] describes the MPC dispersion in delay and angle domains for the non-line-of-sight (NLOS) environments and explores MPC distribution and its propagation mechanisms in different propagation environments. All of those important vehicular channel characteristics show that the vehicular channel exhibits severe fading and statistical nonstationarity. The propagation mechanisms and spatial distributions of MPCs are mainly determined by the vehicular propagation environment.

For the 20–60 GHz band, the studies in [17, 18] show that the large spectrum in a higher frequency band provides a possibility of high data rate, but the channel is much different from that in the 5 GHz band, and directional antennas are adopted by transceivers in such vehicular communication systems to overcome the heavy loss at those high frequencies [19, 20]. But the obvious limitation by using directional antennas for the higher frequency applications is the difficulty of providing an “always connected” V2I or V2V link. In [21], the two-ray channel model with random reflected paths is used to represent 60 GHz vehicular channel, and the system performance has been theoretically evaluated by varying modulation formats, coding complexity, and propagation characteristics for vehicular communications. The similar works in [22, 23] analyze the characteristics of MPC propagation and verify the availability of the vehicular communication system at 60 GHz. Based on channel measurement with rotating directional antennas, the DS, path loss exponent (PLE), and angular spread of arrival (ASA) are compared between line-of-sight (LOS) and NLOS conditions at 60 GHz under outdoor environments in [24, 25]. The channel impulse response and scattering functions, as well as the DS, are obtained from 38 GHz to 60 GHz channel measurements in [26]. Such measurements show that the MPC in the channel typically contains LOS, road reflection paths, and reflection paths from the guard rails. However, the two distinguishing features of vehicular channels at higher frequency bands, e.g., directionality and blockage, are not fully explored in the work, which are the significant challenge remaining in the design of such vehicular networks.

An overview of the previous work is to study the typical behavior of vehicle lanes, identifying missing features in currently available channel models to design and evaluate vehicle radio links in a safe and efficient environment.

In this paper, intensive simulations at the 23 GHz band with 1 GHz bandwidth in a realistic V2I urban environment

are performed by a calibrated ray-tracing (RT) simulator to complement these missing characteristics, e.g., directionality and blockage. Besides, different road widths, traffic flows, vehicle types, antenna heights, and traffic signs are considered in the RT simulation to fully explore the V2I channel behaviors under different conditions. The time-varying power delay profile (PDP), path loss (PL), shadow factor, DS, Ricean K -factor, and angular spreads (ASs)—azimuth angular spread of arrival (ASA), azimuth angular spread of departure (ASD), elevation angular spread of arrival (ESA), and elevation angular spread of departure (ESD)—are analyzed and extracted from the simulation results. In addition, the propagation mechanism in different environments is analyzed that can illustrate the impact of the actual environment on the channel characteristics. Furthermore, the extracted parameters can be input to the channel generator, like QuaDRiGa or METIS, to generate similar channels, which can be used to evaluate or verify the performance of the system- or link-level design.

The rest of this paper is organized as follows: In Section 2, the realistic vehicular environments are reconstructed and introduced. In Section 3, extensive RT simulations are performed in all cases. Then, based on the RT results, the vehicular channels are comprehensively characterized in Section 4. Finally, the conclusions are drawn in Section 5.

2. Realistic Vehicular Moving Network Environments

In order to obtain realistic behavior of vehicular channels in the moving network (MN), the influence of vehicles must be considered in the propagation model [27, 28]. In this paper, to map the MN architecture defined by 3GPP TR 37.885 to the real propagation environments, the 3D models of a set of comprehensive vehicular environments are reconstructed.

2.1. Overview of Environments

2.1.1. Urban Environments. The 3D details of the considered environment are built by OpenStreetMap (OSM). OSM is a collaborative project to create a free editable map of the world, and in addition to street-level map information, it can provide 3D building information. In order to make it easier to access the OSM data, a plugin for SketchUp (3D modeling software) is developed in this work. The plugin can import both street and building information from OSM data. It is the open source software that can be obtained from <http://www.raytracer.cloud/software>. As shown in Figure 1, the typical urban area in Seoul is selected. This urban environment is universal and can represent most of the vehicular propagation environment in the urban area. In addition to OSM, KakaoMap, the Korean map software, is also used to reconstruct the real environment more completely, which has a 360-degree street view, and some landmark buildings such as cafes and restaurants will be specially marked. Combined with OpenStreetMap and KakaoMap, the urban environments in Seoul can be reconstructed by the SketchUp software, which is shown in Figure 2. Considering the

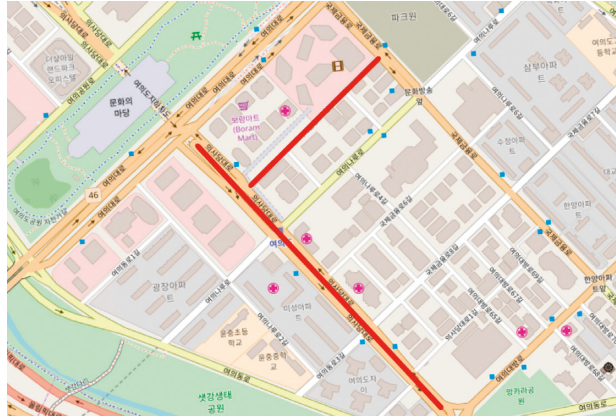


FIGURE 1: Seoul map from OpenStreetMap.

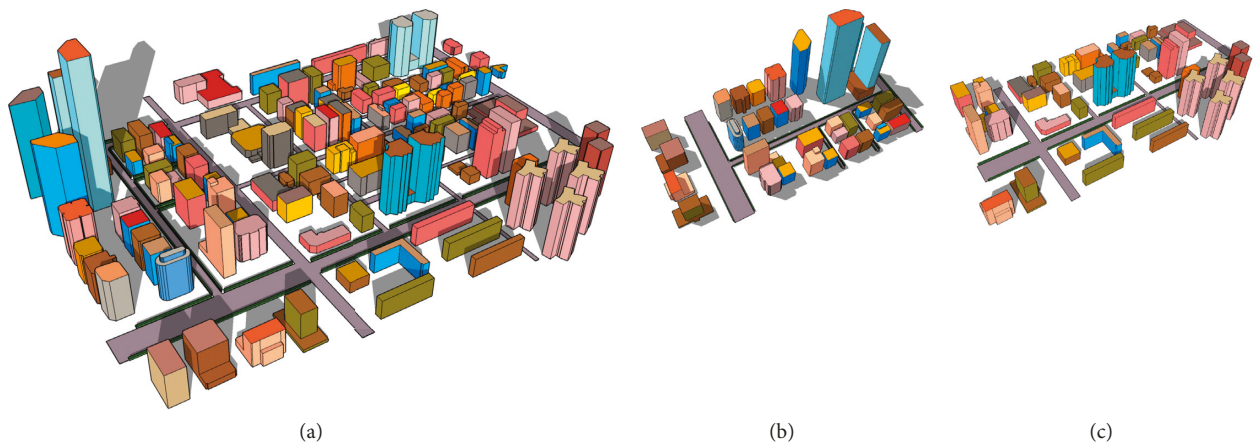


FIGURE 2: (a) 3D model of Seoul urban environment. (b) 3D model of Area 1. (c) 3D model of Area 2.

impact of different neighborhood environments on the vehicular channel, two typical urban streets in the city are selected as the simulation environments. As shown in Figure 1, the selected streets were marked with red lines on the maps. Figures 2(b) and 2(c) show the 3D environment models of these two areas. The difference between the two areas is the width of the road, characterized by the number of lanes.

2.1.2. Small-Scale Structures. In addition to the large buildings, the common small-scale structures such as roadside trees, traffic lights, traffic signs, and bus stations are considered in the environment model. These small-scale structures are on the same order of magnitude as the wavelength, and the most relevant propagation mechanism of them in vehicular environments is scattering [29]. Figure 3 shows the 3D models of small-scale structures in urban environments.

2.2. Vehicle Types and Mobility Modeling

2.2.1. Vehicle Types. In this work, three different vehicle types are selected by considering the recommendation by 3GPP TR 37.885 [30], which are defined as follows:

- (i) Type 1 (passenger vehicle with a lower antenna position): length 5 m, width 2.0 m, height 1.6 m, and antenna height 0.75 m, as shown in Figure 4(a)
 - (ii) Type 2 (passenger vehicle with a higher antenna position): length 5 m, width 2.0 m, height 1.6 m, and antenna height 1.6 m, as shown in Figure 4(a)
 - (iii) Type 3 (truck/bus): length 13 m, width 2.6 m, height 3 m, and antenna height 3 m, as shown in Figure 4(b)
- To more comprehensively reflect the impact of vehicle types on signal propagation, another type of vehicle is also considered:
- (iv) Type 4 (delivery van): length 13.5 m, width 2.6 m, height 3.5 m, and antenna height 3.5 m, as shown in Figure 4(c)

2.2.2. Mobility Modeling. As per the recommendation by 3GPP TR 37.885, the vehicles are dropped for the urban environments according to the following process:

- (i) The distance between the rear bumper of a vehicle and the front bumper of the following vehicle in the same lane follows an exponential distribution
- (ii) All the vehicles in the same lane have the same speed

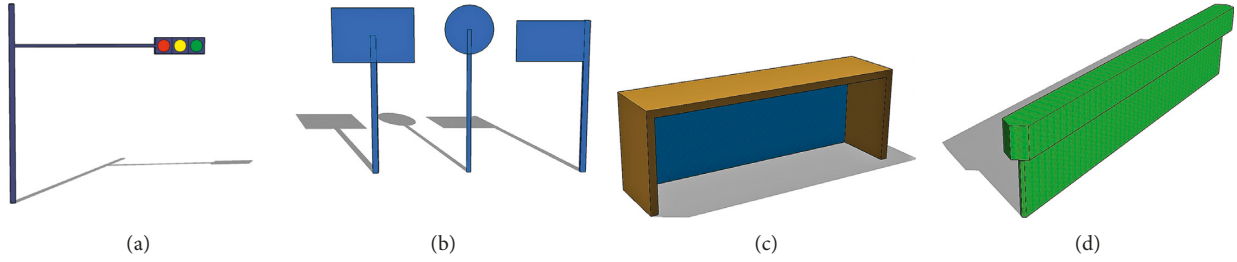


FIGURE 3: 3D models of small-scale structures. (a) Traffic light model. (b) Traffic sign model. (c) Bus station model. (d) Tree model.

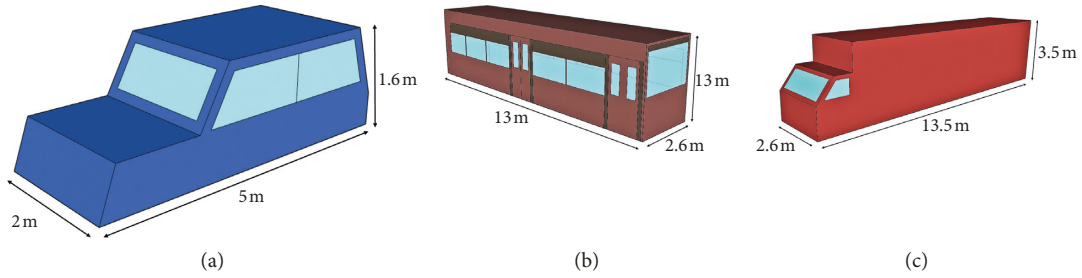


FIGURE 4: 3D models of different vehicle types. (a) Passenger car model. (b) Bus model. (c) Delivery van model.

(iii) Vehicle-type distribution is not dependent on the lane

In general, the width of the line is 3.5 m. In Area 1 (shown in Figure 2(b)), the road is with four lanes. Considering the traffic congestion in the actual environments, the speed and the direction of vehicles in each lane are shown in Figure 5. The width of the road in Area 2, as shown in Figure 2(c), is more extensive than that in Area 1, and the eight-lane road is designed in Area 2. The vehicle speed on such a road is shown in Figure 6. According to the recommendations of 3GPP TR 37.885, the distribution of vehicle types in the urban environment is determined:

- (i) 60% Type 1 vehicles and Type 2 vehicles (passenger car)
- (ii) 20% Type 3 vehicles (bus)
- (iii) 20% Type 4 vehicles (delivery van)

The vehicles in each lane are randomly generated according to vehicle distribution. Vehicles do not change their direction at the intersection.

2.3. Antenna Model. The antennas of the base station (BS) and the user equipment (UE) of the MN system defined are with the same antenna pattern [30], as shown in Figure 7. The locations and heights of the transmitter (Tx) at the BS and receiver (Rx) at the UE are given in Table 1. The settings follow the recommendations of 3GPP TR 37.885.

3. RT Simulations in Realistic Vehicular Scenarios

In this section, in order to characterize the 23 GHz vehicular channels, RT simulations with different antenna height

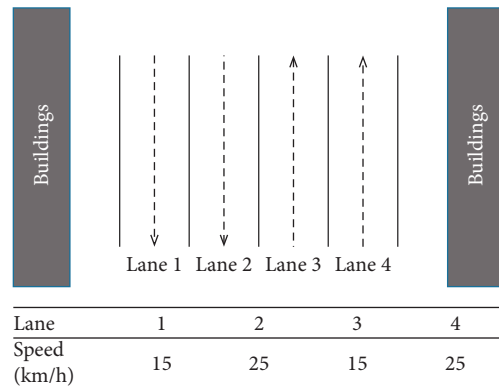


FIGURE 5: Vehicle speed in the 4-lane road (Area 1).

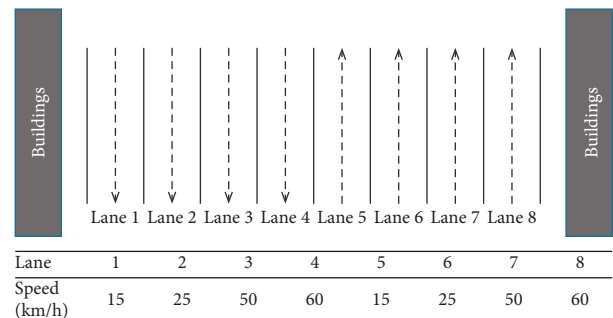


FIGURE 6: Vehicle speed in the 8-lane road (Area 2).

setups are developed in different realistic environment cases. First, the calibration and verification of the RT simulator are discussed, and then the RT configuration and different propagation mechanisms caused by the surrounding environment in various environment cases are presented.

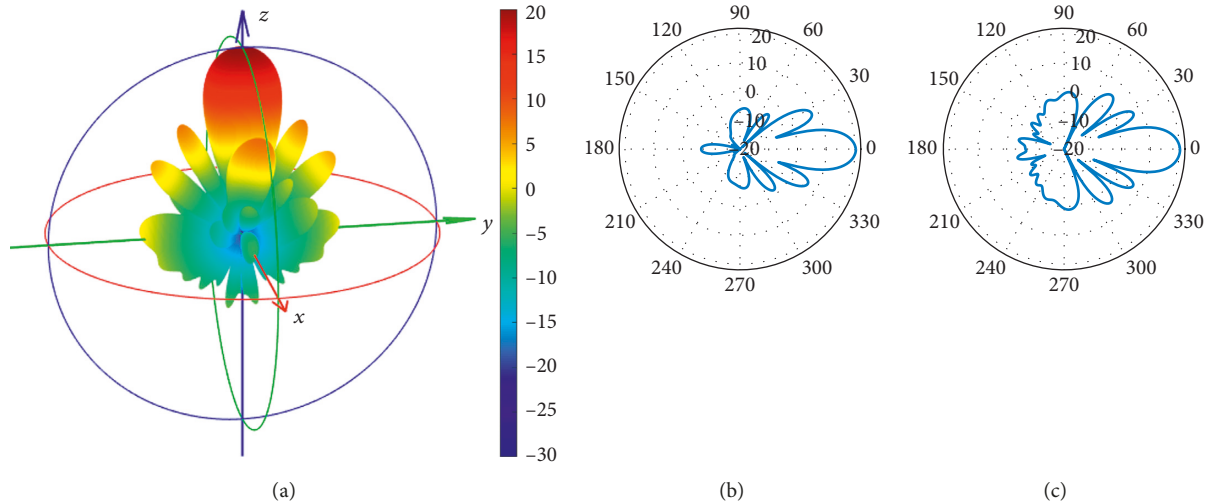


FIGURE 7: (a) 3D antenna pattern of the transceiver. (b) E plane. (c) H plane.

TABLE 1: Locations and heights of the Tx and Rx.

Parameters	Urban
BS antenna height	Top of the building: 25 m On the traffic light: 5 m
UE antenna height	Top of the bus: 3.2 m

3.1. RT Simulation Verification. According to realistic urban 3D maps and design specifications for urban infrastructure, the vehicular environment features, and typical small-scale structures is presented in the above section. Based on which, a large number of statistical consistent environment models can be generated to simulate urban vehicular channels. Before this, RT needs to be calibrated via propagation measurement, and then the intensive close-to-real channel simulations can be conducted with standard-defined configurations.

The validations of the RT simulator against various measurements have been presented in various propagation environments and different frequency bands. For example, RT is calibrated and verified in the tunnel environment at 25 GHz [31], in the urban environment at 28 GHz [28], in the indoor environment at 26 GHz [32], in the viaduct environment at 93 GHz [33], and so on. After the calibration, the corresponding material parameters are obtained. The calibrated materials basically cover all the material composition of the considered propagation environments in this paper, e.g., concrete, brick, granite, marble, glass, and metal. Note that applying appropriate material parameters in RT is a precondition to obtain practical channel results. In general, the material parameters are frequency dependent. The material parameters are calibrated in similar propagation environments at the adjacent frequency band, i.e., 25 GHz and 28 GHz [28, 31]. In Rec. ITU-R P.1238-7 [34] and Rec. ITU-R P.2040 [35], such material parameters for urban and indoor environments can be obtained for 1 GHz–100 GHz, indicate an insignificant difference, and are almost independent of the frequency in the range from 20 GHz to 30 GHz.

3.2. RT Simulation Configuration. Considering the vehicular MN in the urban environment, not only the bus equipped with the Rx can move but also other vehicles such as cars, delivery vans, and other buses can move around as the moving scatterers. Aiming at supporting these features, the workflow is shown in Figure 8. Dynamic mobility patterns of moving objects and the Tx/Rx should be defined prior to simulation. After all the models and configurations are uploaded to the RT simulator, the geometry and visibility relationship of the objects are updated for each snapshot.

The carrier frequency of V2I simulation is 22.6 GHz with a bandwidth of 1 GHz. Both Tx and Rx beam patterns are the same as the Tx antenna beam pattern of the MHN-E system shown in Figure 7. The deployment of the Tx and Rx is shown in Figure 9; the Tx is placed at the top of the building with a height of 25 m or installed on the pillar of the traffic light with a height of 5 m. The Rx is placed on the top of the bus. The travel distance of the bus where the Rx is located is 500 m. The RT simulation includes two simulation granularity settings:

- (i) The low-resolution simulation: with the sampling interval 1.38–1.67 m, it is used to get the channel profile and determine the propagation zones where the high-resolution simulations will take place. Different propagation zones indicate different propagation mechanism combinations.
- (ii) The high-resolution simulation: for every propagation zone in every case, one CIR will be simulated per OFDM symbol duration (which is much shorter than half of the wavelength), in order to feed into the link-level simulator.

The simulation setups are based on the RT frequency-domain method for the ultra-wideband channel, and the material parameters are extracted from measurements or literature. The involved material parameters are summarized in Table 2, where ϵ'_r is the real part of the relative permittivity, $\tan \delta$ is the loss tangent, and S and α are the scattering

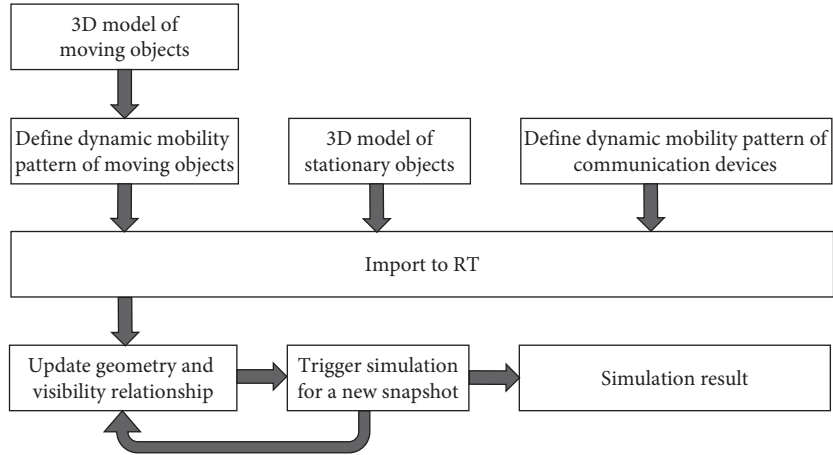


FIGURE 8: Workflow of simulating moving environments.

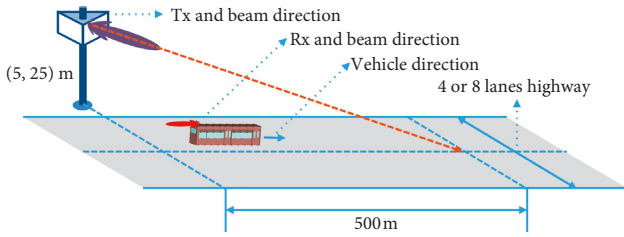


FIGURE 9: Deployment of the Tx and Rx.

coefficient and scattering exponent of the directive scattering model [36]. Particularly, the parameters of wood are calibrated in [37, 38], and the parameters of concrete are calibrated in [39]. Therefore, with the provided calibrated material parameters, various V2I Tx/Rx deployments can be simulated by an RT simulator.

Propagation mechanisms in the simulations are LOS, scattering (multiple scattering theory for vegetation and single-lobe directive model for others), diffraction (uniform theory of diffraction (UTD)), reflection (up to 2 orders), and transmission. The detailed configuration of the RT simulated channels in urban environments is summarized in Table 3. The propagation mechanisms for different objects in the simulation environment are summarized in Table 4.

3.3. Propagation Mechanism Analysis. In this work, 3 different traffic flows are considered:

- (i) Full traffic flow: 100% randomly generated vehicles on the road
- (ii) Half traffic flow: 50% randomly generated vehicles on the road
- (iii) Low traffic flow: 10% randomly generated vehicles on the road

The considered simulation cases are summarized in Table 5 for clarity, and the exemplified simulation results are shown in Figure 10. Figures 10(a) and 10(b) show the MPC distribution of the typical snapshots for Case 9 and Case 10, respectively; moreover, the time-varying PDPs are also given to distinguish the MPC distribution in the delay domain

TABLE 2: Electromagnetic parameters of different materials.

Material	ϵ_r'	$\tan \delta$	S	α
Brick	1.9155	0.0568	0.0019	49.5724
Marble	3.0045	0.2828	0.0022	15.3747
Toughened glass	1.0538	23.9211	0.0025	5.5106
Metal	1	10^7	0.0026	17.7691
Concrete	5.4745	0.0021	0.0011	109
Wood	6.6	0.9394	0.0086	13.1404

intuitively. According to different MPC distribution and propagation mechanisms, the “zone” concept is proposed. Different zones for different cases are used for channel characterization in the next section. For Case 9, three zones can be detected, and two zones are marked for Case 10. According to the RT simulation results for each case, there are 12 typical divided zones in Table 6, in which the details of propagation mechanisms for different zones are listed. For example, in Zone 2, the Rx is out of the Tx main lobe, the LOS path and reflected and scattered paths (from urban furniture and other vehicles) exist, and no ground reflection exists, as shown in Figure 10(c); in Zone 9, the Rx is in the Tx main lobe, LOS and ground reflected paths exist, and no reflection or scattering from urban furniture or other vehicles is seen, as shown in Figure 10(d); in Zone 11, the Rx is in the Tx main lobe and the LOS path is blocked by a vehicle, as shown in Figure 10(e). Note that the rays whose power is more than 80 dB lower than that of the strongest ray are cut off to get the dominant propagation mechanisms.

Extensive high-resolution simulations are conducted in each propagation zone for different cases. All simulated channel data can be imported to the V2I link-level simulator to guide the construction of the vehicular infrastructure for better road services.

4. Key Channel Parameters for Link-Level Simulation

In order to support the link-level simulation, for every propagation zone, the spatial sampling interval is set to 80λ for high-resolution simulation. The delay resolution is

TABLE 3: Environment configuration.

Frequency	22.1–23.1 GHz	
Bandwidth	1 GHz	
Antenna	Directional antenna	
Tx	Power	0 dBm
	Height	5 m, 25 m
Rx	Height	3.2 m
	Travel distance for the urban environment	500 m
V2I path	D1: Rx on lane 2 (4-lane urban street; Figure 5), $v = 25$ km/h	
	D2: Rx on lane 4 (8-lane urban street; Figure 6), $v = 60$ km/h	
Vehicle type	Passenger car	60%
	Bus	20%
	Delivery van	20%
Propagation	Direct	✓
	Reflection	Up to 2 orders
	Diffraction	UTD
	Scattering	Directive scattering model
Material	Transmission	✓
	Building	Brick, marble, toughened glass
	Urban furniture, vehicle	Metal
	Tree	Wood
	Ground, highway fence	Concrete

TABLE 4: Propagation mechanism.

Object	LOS	Reflection (up to 2 orders)	Scattering	Transmission	Diffraction
Trees	✓		✓	✓	
Buildings	✓	✓			✓
Traffic signs	✓	✓			✓
Signal lights	✓	✓			✓
Bus stations	✓	✓			✓
Ground	✓	✓	✓		
Vehicles	✓	✓	✓		✓

TABLE 5: Analysis cases.

Index	Environment	Lane	Tx height (m)	Traffic flow	Terminology
1	Seoul	4	25	Full	Seoul-4Lanes-Tx25-TFFull
2	Seoul	4	25	Half	Seoul-4Lanes-Tx25-TFHalf
3	Seoul	4	25	Low	Seoul-4Lanes-Tx25-TFLow
4	Seoul	4	5	Full	Seoul-4Lanes-Tx5-TFFull
5	Seoul	4	5	Half	Seoul-4Lanes-Tx5-TFHalf
6	Seoul	4	5	Low	Seoul-4Lanes-Tx5-TFLow
7	Seoul	8	25	Full	Seoul-8Lanes-Tx25-TFFull
8	Seoul	8	25	Half	Seoul-8Lanes-Tx25-TFHalf
9	Seoul	8	25	Low	Seoul-8Lanes-Tx25-TFLow
10	Seoul	8	5	Full	Seoul-8Lanes-Tx5-TFFull
11	Seoul	8	5	Half	Seoul-8Lanes-Tx5-TFHalf
12	Seoul	8	5	Low	Seoul-8Lanes-Tx5-TFLow

8.14 ns, and the time sampling rate is 8.92 μ s. Based on extensive RT simulation results, the comprehensive features of 23 lanes in urban environments are analyzed and extracted. The channel characteristics include PL, root-mean-square (RMS) DS, Ricean K -factor (KF), ASA, ASD, ESA, ESD, and blockage loss (BL). All these channel parameters are fitted by the normal distribution with the mean value and standard deviation. All the extracted parameters are summarized in Tables 7–9, where μ DS, μ KF, μ ASA, μ ASD, μ ESA, and μ ESD are the mean values of DS, KF, ASA,

ASD, ESA, and ESD, respectively. σ DS, σ KF, σ ASA, σ ASD, σ ESA, and σ ESD are the standard deviations of DS, KF, ASA, ASD, ESA, and ESD, respectively.

4.1. *Path Loss.* The PL in dB is modeled by the A-B model, which is expressed as

$$PL(dB) = A \cdot \log_{10}\left(\frac{d}{d_0}\right) + B + X_{\sigma}, \quad (1)$$

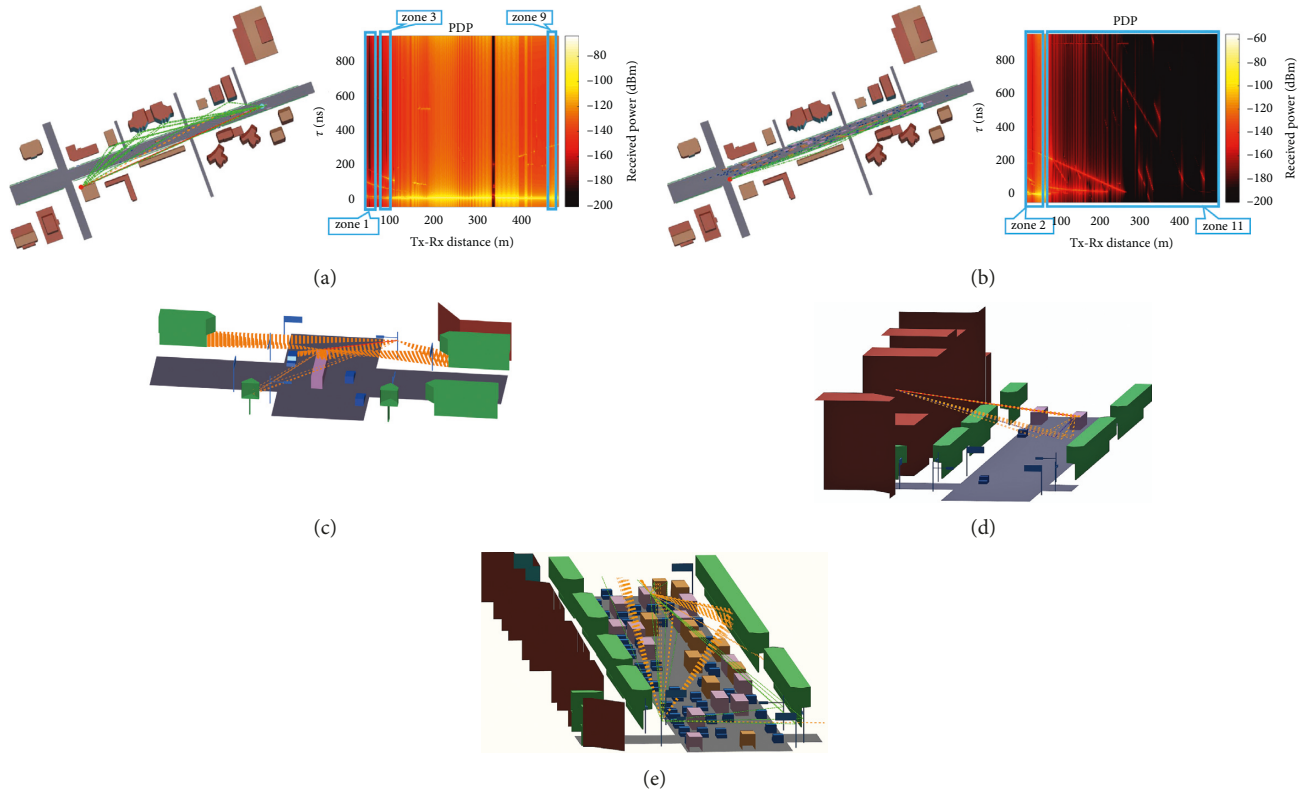


FIGURE 10: Exemplified RT simulation results in different cases and zones. (a) Case 9: Seoul-8Lanes-Tx25-TFLow. (b) Case 10: Seoul-8Lanes-Tx5-TFFull. (c) One typical snapshot of Zone 2. (d) One typical snapshot of Zone 9. (e) One typical snapshot of Zone 11.

TABLE 6: Zones of simulation results.

Zone	Antenna alignment	LOS condition			Propagation mechanism	
		LOS	Blocked by vehicle	NLOS Blocked by urban furniture	Ground reflection	Reflection/scattering from urban furniture and other vehicles
1	×	✓	×	×	×	×
2	×	✓	×	×	×	✓
3	×	✓	×	×	✓	×
4	×	✓	×	×	✓	✓
5	×	×	✓	×	—	—
6	×	×	×	✓	—	—
7	✓	✓	×	×	×	×
8	✓	✓	×	×	×	✓
9	✓	✓	×	×	✓	×
10	✓	✓	×	×	✓	✓
11	✓	×	✓	×	—	—
12	✓	×	×	✓	—	—

✓: within main lobe; ×: outside main lobe.

where d is the distance between the Tx and the Rx in m; d_0 is the reference distance, equal to 1 m; A is the PL exponent; B is the offset; and X_σ is the shadow factor (SF), which can be modeled as a Gaussian variable with zero mean and a standard deviation σ_{SF} .

The fitting results of all 23 zones for different analysis cases are listed in Table 7, where $A < 0$ is under the conditions that the Tx and Rx antenna beams are misaligned at

the beginning and that the moving Rx gradually approached the main lobe of the Tx. The similar result is presented in the previous work [31]. It can be found that the absolute value of A in Zone 1 to Zone 4 (outside the main lobe of the Tx and LOS condition) and Zone 11 and Zone 12 (within the main lobe of the Tx and NLOS condition) is larger than that in Zone 7 to Zone 10 (within the main lobe of the Tx and LOS condition). This indicates that the main lobe and the

TABLE 7: Extracted parameters for the PL.

Environment	Zone	PL (dB)		σ_{SF}
		A	B	
Seoul-4Lanes-Tx25-TFFull	8	10.71	37.32	1.14
	10	-415.00	1104.00	3.69
Seoul-4Lanes-Tx25-TFLow	1	-96.78	271.93	0.29
	9	24.39	3.47	4.36
Seoul-4Lanes-Tx5-TFFull	8	29.81	-11.58	0.84
	2	141.50	-31.47	3.17
Seoul-4Lanes-Tx5-TFHalf	10	5.37	47.69	5.37
	1	34.54	56.56	5.44
Seoul-4Lanes-Tx5-TFLow	3	-77.27	152.50	2.60
	2	135.07	-122.46	4.21
Seoul-8Lanes-Tx25-TFFull	8	7.40	46.50	0.84
	12	1674	-4100	10.46
Seoul-8Lanes-Tx25-TFHalf	1	-243.70	497.19	3.96
	4	30.19	44.80	1.51
Seoul-8Lanes-Tx25-TFLow	7	-46.56	170.31	0.59
	3	-374.55	760.65	7.22
Seoul-8Lanes-Tx5-TFFull	9	62.08	-97.05	5.33
	2	-58.31	158.92	5.28
Seoul-8Lanes-Tx5-TFHalf	11	90.38	-71.97	15.06
	8	14.89	25.98	2.71
Seoul-8Lanes-Tx5-TFLow	4	-61.72	164.97	6.10
	10	12.85	30.87	5.89

barriers, i.e., other vehicles and traffic signs, have a great influence on path loss. With the increase of traffic flow, the probability of occurrence of Zone 5 and Zone 11 (LOS path is blocked by other vehicles) rises.

4.2. RMS DS and Ricean K-Factor. The Ricean K -factor is defined as the ratio of the power of the strongest MPC to the power of the sum of the remaining MPCs in the received signal [40]. Traditionally, the Ricean K -factor is calculated from the narrowband channel sounding results by using a moment-based method [41]. However, the ultra-wideband (UWB) channel sounding results in this measurement have high resolution in the time domain. Thus, the Ricean K -factor can be calculated according to its definition as follows:

$$KF = 10 \cdot \log_{10} \left(\frac{P_{\text{strongest}}}{\sum P_{\text{remaining}}} \right), \quad (2)$$

where KF denotes the Ricean K -factor and $P_{\text{strongest}}$ and $P_{\text{remaining}}$ denote the power of the strongest MPC and the power of the remaining MPCs, respectively. RMS DS is used to quantify the dispersion effect of the wide channel. It is defined as the square root of the second central moment of the PDP [42]:

$$\sigma_{\tau} = \sqrt{\frac{\sum_{n=1}^N \tau_n^2 \cdot P_n}{\sum_{n=1}^N P_n} - \left(\frac{\sum_{n=1}^N \tau_n \cdot P_n}{\sum_{n=1}^N P_n} \right)^2}, \quad (3)$$

TABLE 8: Extracted parameters for the DS and K -factor.

Environment	Zone	DS (ns)		KF (dB)	
		μ_{DS}	σ_{DS}	μ_{KF}	σ_{KF}
Seoul-4Lanes-Tx25-TFFull	8	1.39	0.23	52.26	15.46
	10	2.30	1.06	27.38	27.50
Seoul-4Lanes-Tx25-TFLow	1	1.29	0.01	47.23	6.04
	9	4.77	2.04	23.60	20.81
Seoul-4Lanes-Tx5-TFFull	12	81.32	83.08	0.47	6.82
	8	1.77	0.21	44.22	4.07
Seoul-4Lanes-Tx5-TFHalf	2	19.42	4.73	-1.37	1.67
	10	5.44	0.87	42.04	3.96
Seoul-4Lanes-Tx5-TFLow	1	17.28	7.08	2.81	3.48
	3	14.54	9.48	7.94	9.14
Seoul-8Lanes-Tx25-TFFull	2	23.95	8.42	9.79	5.30
	8	1.89	1.35	44.23	10.64
Seoul-8Lanes-Tx25-TFHalf	12	75.4	42.14	-4.55	12.89
	1	28.17	12.52	10.74	5.74
Seoul-8Lanes-Tx25-TFLow	4	16.36	4.41	7.58	3.22
	7	2.60	1.04	41.54	4.29
Seoul-8Lanes-Tx5-TFFull	3	32.1	4.65	2.07	2.84
	9	4.00	0.37	38.21	2.22
Seoul-8Lanes-Tx5-TFHalf	2	8.17	11.72	25.16	17.74
	11	46.54	66.15	0.74	15.21
Seoul-8Lanes-Tx5-TFLow	8	2.84	3.36	56.32	15.16
	4	13.19	17.37	11.77	7.67
Seoul-8Lanes-Tx5-TFLow	10	9.07	3.46	53.24	15.13

where σ_{τ} denotes the RMS delay spread and P_n and τ_n denote the power and the excess delay of the n -th multipath. The fitting parameters for KF and σ_{τ} are listed in Table 8.

As it can be seen from Table 8, the zones with the LOS path are outside the main lobes of transceivers (as shown in Figure 11), the Ricean K -factor is smaller than that of the zones with the LOS path in such main lobes, yet the delay spread is larger than that in the zones with the LOS path in the main lobes. The reason is that the MPCs in the main lobes would have higher gain than the LOS path which gives rise to increasing $P_{\text{remaining}}$ with a long delay. Another finding is that, in the case of the same environment, i.e., the same Tx height and the same zone, the mean value of Ricean K -factor in full traffic flow is smaller than that under the half and low traffic flow conditions; meanwhile, the mean value of DS is larger. As shown in Figure 12, there are more MPCs caused by more vehicles in the case of full traffic flow, resulting in an increase in power to diffuse MPCs. As shown in Figure 13, the Ricean K -factor in some cases of the NLOS channel with reflection is larger than that in other cases of the NLOS channel without reflection. The channel with the strongly reflected path is close to the cases of the LOS channel. It has been found that such strong reflected paths are mainly from a metal vehicle or the ground, and power of them is almost as strong as the LOS path.

4.3. Angular Spread. According to the 3GPP definition, the conventional AS calculation for the composite signal is given by

TABLE 9: Extracted parameters for the AS.

Environment	Zone	ASA (°)		ESA (°)		ASD (°)		ESD (°)	
		μ_{ASA}	σ_{ASA}	μ_{ESA}	σ_{ESA}	μ_{ASD}	σ_{ASD}	μ_{ESD}	σ_{ESD}
Seoul-4Lanes-Tx25-TFFull	8	0.14	0.21	0.42	1.33	0.19	0.03	0.05	0.17
	10	0.03	0.00	2.28	2.13	0.19	0.10	0.29	0.10
Seoul-4Lanes-Tx25-TFLow	1	0.07	0.01	0.02	0.00	0.30	0.03	0.00	0.00
	9	0.37	0.83	3.27	1.10	0.26	0.29	0.42	0.14
	12	143.83	29.62	2.04	0.58	7.48	9.69	0.57	0.04
Seoul-4Lanes-Tx5-TFFull	8	1.55	0.57	0.11	0.18	0.00	0.00	0.01	0.02
Seoul-4Lanes-Tx5-TFHalf	2	52.11	27.11	18.06	1.59	72.27	13.14	8.26	1.69
	10	1.37	0.10	1.24	0.14	0.00	0.00	0.80	0.09
Seoul-4Lanes-Tx5-TFLow	1	43.55	26.66	18.28	1.70	72.67	12.85	8.37	1.78
	3	47.28	41.54	12.06	6.69	40.63	32.22	8.39	5.44
Seoul-8Lanes-Tx25-TFFull	2	46.97	11.44	24.65	3.66	1.23	0.40	2.13	0.59
	8	6.54	31.00	0.22	1.00	0.09	0.23	0.04	0.06
	12	52.62	25.63	2.53	1.34	3.68	1.50	0.42	0.15
Seoul-8Lanes-Tx25-TFHalf	1	39.26	9.23	24.85	3.68	1.17	0.50	2.07	0.65
	4	79.11	28.25	10.02	2.53	3.93	1.10	0.55	0.24
	7	0.27	0.29	0.01	0.00	0.16	0.10	0.05	0.00
Seoul-8Lanes-Tx25-TFLow	3	98.51	18.6	21.54	1.06	7.25	0.73	3.62	0.65
	9	0.01	0.00	2.90	0.06	0.01	0.00	0.37	0.01
Seoul-8Lanes-Tx5-TFFull	2	22.72	35.31	2.73	4.84	8.62	10.32	1.78	1.89
	11	28.98	31.14	1.01	0.75	2.45	3.07	0.77	1.36
Seoul-8Lanes-Tx5-TFHalf	8	14.16	46.64	0.07	0.25	0.10	0.25	0.05	0.11
Seoul-8Lanes-Tx5-TFLow	4	21.78	35.13	4.71	4.34	10.82	11.74	4.22	3.55
	10	0.01	0.01	0.90	0.15	0.01	0.00	0.58	0.10

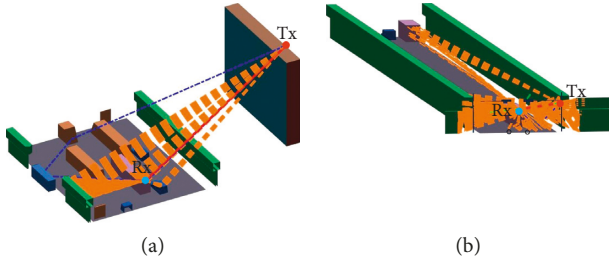


FIGURE 11: Rays in the main lobes of the transceiver. (a) Reflected rays aligned with the main lobe. (b) Scattered rays aligned with the main lobe.

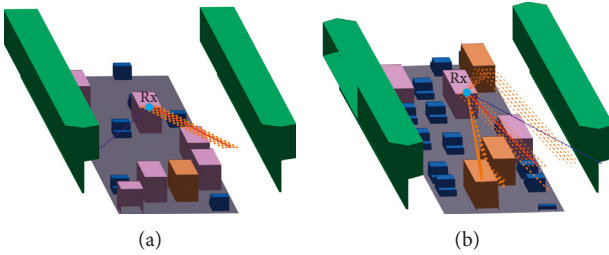


FIGURE 12: MPC distribution in the same environment with different traffic flows. (a) Zone 8 in Case 2 (Seoul-4Lanes-Tx25-TFHalf). (b) Zone 8 in Case 1 (Seoul-4Lanes-Tx25-TFFull).

$$\sigma_{AS} = \sqrt{\frac{\sum_{n=1}^N (\theta_{n,\mu})^2 \cdot P_n}{\sum_{n=1}^N P_n}}, \quad (4)$$

where σ_{AS} denotes the AS, P_n denotes the power of the n -th ray, and $\theta_{n,\mu}$ is defined by

$$\theta_{n,\mu} = \text{mod}(\theta_n - \mu_\theta + \pi, 2\pi) - \pi, \quad (5)$$

where θ_n is the ASA/ASD/ESA/ESD of the n -th ray and μ_θ is

$$\mu_\theta = \frac{\sum_{n=1}^N \theta_n \cdot P_n}{\sum_{n=1}^N P_n}. \quad (6)$$

Generally speaking, ASD and ASA are larger than ESD and ESA, implying that most of the MPCs come from the horizontal direction. This reflects the fact that more objects (scatterers) are located on the two sides of the Rx vehicle in the urban environment than above/under the Rx vehicle (as shown in Figure 14). Figure 15 shows the variation of the AS with Tx-Rx distance for the urban environment. It can be seen that, in the case of the LOS channel, the mean value of angular spread within the main lobe is generally smaller than that outside the main lobe. This indicates that when the Rx is within the main lobe, the distance between the Rx and the Tx is larger, and the object that produces reflection and scattering is closer to the Tx than the Rx. Moreover, the main lobe filters low-energy rays, resulting in the reduced AS.

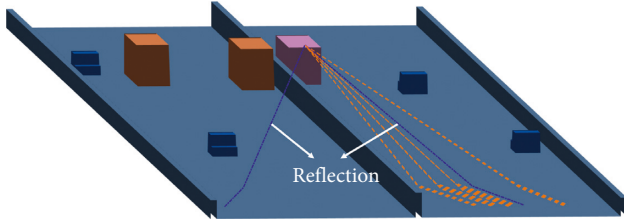


FIGURE 13: NLOS channel with the strong reflected path.

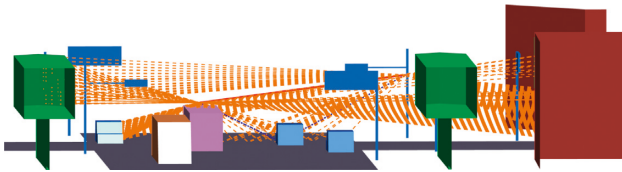


FIGURE 14: MPC spatial distribution in the vehicular channel in urban environments.

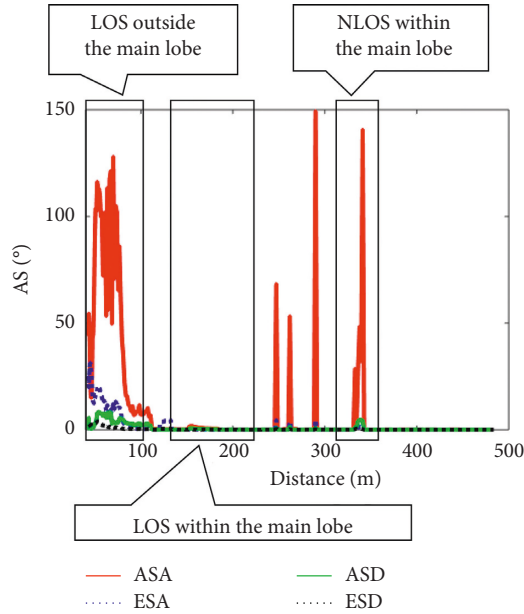


FIGURE 15: AS of urban environments in both azimuth and elevation domains.

Another finding is that when the Rx vehicle is within the main lobe, the AS for NLOS channels is much larger than that for LOS channels.

4.4. Blockage Loss. There are buildings, small-scale structures, and moving vehicles in the analyzed urban environments. When the vehicle on which the Rx is located is moving on the road, the directed ray may be blocked by these objects. As shown in Figure 16, the maximum blockage loss and the corresponding blockage time for each segment are calculated and fitted by the normal distribution with the mean value μBL , σBL_t , and standard deviation μBL , σBL_t , respectively. The parameters are summarized in Table 10.

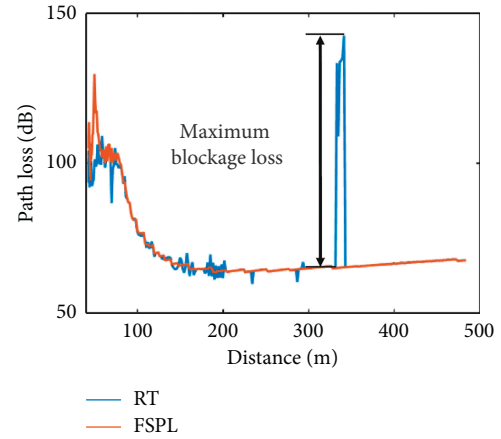


FIGURE 16: An example of blockage loss, RT, raytracing; FSPL, free space path loss.

TABLE 10: Extracted parameters for the blockage loss.

μBL (dB)	σBL (dB)	μBL_t (s)	σBL_t (s)
59.75	35.94	2.76	5.67

5. Conclusion

In this paper, the 23 GHz V2I channels are characterized by measurement-validated RT simulations for different antenna heights in various propagation environments. The PL, shadow fading, Ricean K -factor, DS, AS, and blockage loss of the channels are characterized for each zone in different cases. In the considered 3D Seoul urban environments, all the main buildings and small-scale structures, such as traffic lights, traffic signs, bus stations, and trees, are included with their typical geometries and materials in reality. The fundamental channel parameters analyzed are summarized in tables, which can be imported to standard channel models for generating realistic channels for similar environments. The study of this paper and the provided suggestions will be useful to guide the design and deployment of vehicular communication systems with FACS technologies.

Data Availability

The environment models and simulation data of this study are available from the corresponding author upon request.

Conflicts of Interest

The authors declare that they have no conflicts of interest.

Acknowledgments

This work was supported by the National Key Research and Development program under Grant 2016YFE0200900, NSFC under Grants 61771036, U1834210, and 61725101, Newton Fund under Grant 6181101396, Beijing Natural Science Foundation under Grant L161009, Beijing Natural Haidian Joint Fund under Grant L172020, major projects of Beijing Municipal Science and Technology Commission under Grant Z181100003218010, Fundamental Research

Funds for the Central Universities under Grants 2017RC031, 2018RC030, and 2019JBM074, State Key Lab of Rail Traffic Control and Safety under Grants RCS2018ZZ007 and RCS2019ZZ005, and Teaching Reform Project under Grant 134496522.

References

- [1] A. Molisch, F. Tufvesson, J. Karedal, and C. Mecklenbrauker, "A survey on vehicle-to-vehicle propagation channels," *IEEE Wireless Communications*, vol. 16, no. 6, pp. 12–22, 2009.
- [2] T. Hwang, S. Kang, and H. Hong, "Technical analysis for flexible access common spectrum (FACS)," in *Proceedings of the 2006 International Symposium on Communications and Information Technologies*, pp. 1000–1003, Bangkok, Thailand, October 2006.
- [3] T. Sukuvaara and P. Nurmi, "Wireless traffic service platform for combined vehicle-to-vehicle and vehicle-to-infrastructure communications," *IEEE Wireless Communications*, vol. 16, no. 6, pp. 54–61, 2009.
- [4] X. Chen, S. Guo, and Q. Wu, "Link-level analysis of a multiservice indoor distributed antenna system [wireless corner]," *IEEE Antennas and Propagation Magazine*, vol. 59, no. 3, pp. 154–162, 2017.
- [5] K. Guan, D. He, B. Ai et al., "5-GHz obstructed vehicle-to-vehicle channel characterization for internet of intelligent vehicles," *IEEE Internet of Things Journal*, vol. 6, no. 1, pp. 100–110, 2019.
- [6] J. Kurner, N. Czink, A. Paier, F. Tufvesson, and A. F. Molisch, "Path loss modeling for vehicle-to-vehicle communications," *IEEE Transactions on Vehicular Technology*, vol. 60, no. 1, pp. 323–328, 2011.
- [7] L. Cheng, B. Henty, D. Stancil, F. Bai, and P. Mudalige, "Mobile vehicle-to-vehicle narrow-band channel measurement and characterization of the 5.9 GHz dedicated short range communication (DSRC) frequency band," *IEEE Journal on Selected Areas in Communications*, vol. 25, no. 8, pp. 1501–1516, 2007.
- [8] O. Renaudin, V. Kolmonen, P. Vainikainen, and C. Oestges, "Wideband MIMO car-to-car radio channel measurements at 5.3 GHz," in *Proceedings of the 2008 IEEE 68th Vehicular Technology Conference*, pp. 1–5, Calgary, Canada, September 2008.
- [9] X. Chen, S. Zhang, and Q. Li, "A review of mutual coupling in MIMO systems," *IEEE Access*, vol. 6, pp. 24706–24719, 2018.
- [10] A. Paier, J. Karedal, N. Czink et al., "Car-to-car radio channel measurements at 5 GHz: pathloss, power-delay profile, and delay-doppler spectrum," in *Proceedings of the 2007 4th International Symposium on Wireless Communication Systems*, pp. 224–228, Trondheim, Norway, October 2007.
- [11] A. Paier, J. Karedal, N. Czink et al., "First results from car-to-car and car-to-infrastructure radio channel measurements at 5.2 GHz," in *Proceedings of the 2007 IEEE 18th International Symposium on Personal, Indoor and Mobile Radio Communications*, pp. 1–5, Athens, Greece, September 2007.
- [12] X. Cheng, Q. Yao, M. Wen, C. Wang, L. Song, and B. Jiao, "Wideband channel modeling and intercarrier interference cancellation for vehicle-to-vehicle communication systems," *IEEE Journal on Selected Areas in Communications*, vol. 31, no. 9, pp. 434–448, 2013.
- [13] R. He, O. Renaudin, V.-M. Kolmonen et al., "A dynamic wideband directional channel model for vehicle-to-vehicle communications," *IEEE Transactions on Industrial Electronics*, vol. 62, no. 12, pp. 7870–7882, 2015.
- [14] T. Abbas, L. Bernado, A. Thiel, C. Mecklenbrauker, and F. Tufvesson, "Radio channel properties for vehicular communication: merging lanes versus urban intersections," *IEEE Vehicular Technology Magazine*, vol. 8, no. 4, pp. 27–34, 2013.
- [15] R. He, A. F. Molisch, F. Tufvesson, Z. Zhong, B. Ai, and T. Zhang, "Vehicle-to-vehicle propagation models with large vehicle obstructions," *IEEE Transactions on Intelligent Transportation Systems*, vol. 15, no. 5, pp. 2237–2248, 2014.
- [16] R. He, O. Renaudin, V.-M. Kolmonen et al., "Vehicle-to-vehicle radio channel characterization in crossroad scenarios," *IEEE Transactions on Vehicular Technology*, vol. 65, no. 8, pp. 5850–5861, 2016.
- [17] T. S. Rappaport, G. R. MacCartney, M. K. Samimi, and S. Sun, "Wideband millimeter-wave propagation measurements and channel models for future wireless communication system design," *IEEE Transactions on Communications*, vol. 63, no. 9, pp. 3029–3056, 2015.
- [18] W. Fan, F. Zhang, and G. F. Pedersen, "Validation of test environment in simple sectorized MPAC setups for over-the-air testing of 5G communication systems," *IEEE Antennas and Propagation Magazine*, vol. 16, no. 3, 2019.
- [19] I. Sen and D. W. Matolak, "Vehicle-vehicle channel models for the 5-GHz band," *IEEE Transactions on Intelligent Transportation Systems*, vol. 9, no. 2, pp. 235–245, 2008.
- [20] C. Wang, X. Cheng, and D. I. Laurenson, "Vehicle-to-vehicle channel modeling and measurements: recent advances and future challenges," *IEEE Communications Magazine*, vol. 47, no. 11, pp. 96–103, 2009.
- [21] O. Andrisano, M. Chiani, M. Frullone, C. Moss, and V. Tralli, "Propagation effects and countermeasures analysis in vehicle-to-vehicle communication at millimeter waves," in *Proceedings of the Vehicular Technology Society 42nd VTS Conference—Frontiers of Technology*, vol. 1, pp. 312–316, Denver, CO, USA, May 1992.
- [22] A. Kato, K. Sato, M. Fujise, and S. Kawakami, "Propagation characteristics of 60-GHz millimeter waves for ITS inter-vehicle communications," *IEICE Transactions on Communications*, vol. 84, no. 9, pp. 2530–2539, 2001.
- [23] T. Wada, M. Maeda, M. Okada, K. Tsukamoto, and S. Komaki, "Theoretical analysis of propagation characteristics in millimeter-wave intervehicle communication system," *Electronics and Communications in Japan (Part II: Electronics)*, vol. 83, no. 11, pp. 33–43, 2000.
- [24] E. Ben-Dor, T. S. Rappaport, Y. Qiao, and S. J. Lauffenburger, "Millimeter-wave 60 GHz outdoor and vehicle AOA propagation measurements using a broadband channel sounder," in *Proceedings of the IEEE Global Telecommunications Conference—GLOBECOM 2011*, pp. 1–6, Houston, TX, USA, December 2011.
- [25] J. Zhang, Y. Zhang, Y. Yu, R. Xu, Q. Zheng, and P. Zhang, "3-D MIMO: how much does it meet our expectations observed from channel measurements?," *IEEE Journal on Selected Areas in Communications*, vol. 35, no. 8, pp. 1887–1903, 2017.
- [26] M. G. Sánchez, M. P. Táboas, and E. L. Cid, "Millimeter wave radio channel characterization for 5G vehicle-to-vehicle communications," *Measurement*, vol. 95, pp. 223–229, 2017.
- [27] K. Guan, D. He, B. Ai et al., "Realistic channel characterization for 5G millimeter-wave railway communications," in *Proceedings of the 2018 IEEE Globecom Workshops (GC Wkshps)*, pp. 1–6, Abu Dhabi, UAE, December 2018.
- [28] D. He, B. Ai, K. Guan, L. Wang, Z. Zhong, and T. Kurner, "The design and applications of high-performance ray-tracing simulation platform for 5G and beyond wireless

- communications: a tutorial,” *IEEE Communications Surveys & Tutorials*, vol. 21, no. 1, pp. 10–27, 2019.
- [29] K. Guan, B. Ai, B. Peng et al., “Towards realistic high-speed train channels at 5G millimeter-wave band—part I: paradigm, significance analysis, and scenario reconstruction,” *IEEE Transactions on Vehicular Technology*, vol. 67, no. 10, pp. 9112–9128, 2018.
- [30] “Study on evaluation methodology of new vehicle-to-everything (V2X) use cases for LTE and NR (Release 15), 3rd Generation Partnership Project (3GPP) TR 37.885-15.0.0,” June 2018.
- [31] D. He, B. Ai, K. Guan et al., “Channel measurement, simulation, and analysis for high-speed railway communications in 5G millimeter-wave band,” *IEEE Transactions on Intelligent Transportation Systems*, vol. 19, no. 10, pp. 3144–3158, 2018.
- [32] B. Ai, K. Guan, R. He et al., “On indoor millimeter wave massive MIMO channels: measurement and simulation,” *IEEE Journal on Selected Areas in Communications*, vol. 35, no. 7, pp. 1678–1690, 2017.
- [33] J. Yang, B. Ai, K. Guan et al., “A geometry-based stochastic channel model for the millimeter-wave band in a 3GPP high-speed train scenario,” *IEEE Transactions on Vehicular Technology*, vol. 67, no. 5, pp. 3853–3865, 2018.
- [34] ITU-R, *P.1238-7: Propagation Data and Prediction Methods for the Planning of Indoor Radiocommunication Systems and Radio Local Area Networks in the Frequency Range 900 MHz to 100 GHz*, ITU Recommendations, Geneva, Switzerland, 2012.
- [35] ITU-R, *P.2040: Effects of Building Materials and Structures on Radiowave Propagation above about 100 MHz*, ITU Recommendations, Geneva, Switzerland, 2013.
- [36] V. Degli-Esposti, F. Fuschini, E. M. Vitucci, and G. Falciasacca, “Measurement and modelling of scattering from buildings,” *IEEE Transactions on Antennas and Propagation*, vol. 55, no. 1, pp. 143–153, 2007.
- [37] F. Wang and K. Sarabandi, “An enhanced millimeter-wave foliage propagation model,” *IEEE Transactions on Antennas and Propagation*, vol. 53, no. 7, pp. 2138–2145, 2005.
- [38] H. M. Rahim, C. Y. Leow, and T. A. Rahman, “Millimeter wave propagation through foliage: comparison of models,” in *Proceedings of the 2015 IEEE 12th Malaysia International Conference on Communications (MICC)*, pp. 236–240, Kuching, Malaysia, November 2015.
- [39] K. Guan, B. Ai, B. Peng et al., “Towards realistic high-speed train channels at 5G millimeter-wave band: part II: case study for paradigm implementation,” *IEEE Transactions on Vehicular Technology*, vol. 67, no. 10, pp. 9129–9144, 2018.
- [40] L. Bernado, T. Zemen, F. Tufvesson, A. F. Molisch, and C. F. Mecklenbrauker, “Time- and frequency-varying K-factor of non-stationary vehicular channels for safety-relevant scenarios,” *IEEE Transactions on Intelligent Transportation Systems*, vol. 16, no. 2, pp. 1007–1017, 2015.
- [41] T. Zhou, C. Tao, S. Salous, L. Liu, and Z. Tan, “Channel characterization in high-speed railway station environments at 1.89 GHz,” *Radio Science*, vol. 50, no. 11, pp. 1176–1186, 2015.
- [42] T. Rappaport, *Wireless Communications: Principles and Practice*, Prentice-Hall, Upper Saddle River, NJ, USA, 2002.



Hindawi

Submit your manuscripts at
www.hindawi.com

